Article

Dynamic Recrystallization, Texture Evolution, and Improved Mechanical Properties of Mg-Y-Zn-V Alloy during Forging and Subsequent Extruding Deformation

Wenjie Liu [1], Changjiang Zhang [1,2,*], Qun Shi [1], Fuyin Han [1] and Peng Cao [3,*]

[1] College of Materials Science and Engineering, Taiyuan University of Technology, Taiyuan 030024, China; liuwenjie0318@link.tyut.edu.cn (W.L.); 17862935158@126.com (Q.S.); hanfuyin@tyut.edu.cn (F.H.)

[2] Engineering Research Center of Advanced Metal Composites Forming Technology and Equipment, Ministry of Education, Taiyuan 030024, China

[3] Department of Chemical and Materials Engineering, The University of Auckland, 10 Private Bag 92019, Auckland 1142, New Zealand

* Correspondence: zhangchangjiang@tyut.edu.cn (C.Z.); p.cao@auckland.ac.nz (P.C.)

Abstract: In this paper, the electron backscatter diffraction (EBSD) technique was used to analyze the dynamic recrystallization (DRX), twinning, slip behavior, and texture evolution during forging and subsequent extruding deformation. The results show that, as the degree of strain increased (forging to extruding), the degree of DRX increased, and the DRX mechanism changed from discontinuous DRX (DDRX) during forging to DDRX and continuous DRX (CDRX) during extruding. Particle stimulation nucleation (PSN) promoting DRX occurred during deformation. The deformation process mainly produced {10–12} twins (TTW) and played a role in coordinating the deformation. The slip behavior also changed according to an analysis of in-grain misorientation axes (IGMA) results, changing from slip-dominated with a basal <a> slip to co-dominated with multiple slip modes, with the activation of mainly prismatic <a> and pyramidal <c+a> slip. Meanwhile, the strong basal texture at the beginning of the deformation also changed, and the texture strength decreased from 24.81 to 15.56. The weakening of the texture was mainly due to the formation of DRX grains and twins, as the newly formed DRX and twins reoriented. In the later stages of deformation, the activation of prismatic <a> slip and pyramidal <c+a> slip changed the basal texture component. Based on microstructural analysis, the improvement in mechanical properties was due to fine-grain strengthening and load-transfer strengthening. The ultimate tensile strength (UTS) was 370.5 MPa, the yield strength (YS) was 340.1 MPa, and the elongation (EL) was 15.6%.

Keywords: Mg-Y-Zn-V alloy; DRX; texture; twinning; slip behavior; mechanical properties

1. Introduction

As a lightweight metal structural material, Mg alloys are favored in the transportation industry, such as for automobiles [1–3]. However, most Mg alloys (hexagonal close-packed (HCP) structure) are difficult to process due to their poor ductile deformation ability at room temperature, resulting in greatly limited properties and application ranges. Mg alloys produce strong basal plane weaving, leading to strong anisotropy during low-temperature deformation due to the low number of slip systems. Hence, it becomes important to study the deformation behavior of magnesium alloys.

Twinning is the important deformation mechanism in Mg alloys. The twinning effect on the strength and ductility of an alloy cannot be ignored. Barnett argued that a twin (which provides extension along the c-axis) can increase the uniform elongation in tensile tests [4]. Additional deformation modes of magnesium alloys during low-temperature deformation are provided via deformation twins [5,6]. Commonly observed deformation twins include {10–12} tensile twins (TTW), {10–11} compression twins (CTW), and

{10–11}–{10–12} double twins (DTW), of which TTW are readily activated to coordinate deformation [7]. Twin boundaries (TBs) can divide the initial grains through the intersecting action of the twins. Most studies suggest that CTW and DTW can stimulate DRX formation and split grain [8–10]. Conversely, TTWs cannot stimulate DRX formation because they can grow rapidly [9]. Concurrently, twinning exists in a variety of variants, especially TTW twins, and different twinning have a great influence on the microstructure and properties. Gui et al. [11] studied twinning behavior at room temperature. The results show that three variant types exist and interact with each other, with multiple variant cross-structures restricting the twin grain growth process. Twins can change the texture of magnesium alloys while increasing their strength and plasticity. Therefore, studying the twinning behavior during deformation is necessary.

Every magnesium alloy grain has an HCP structure. At room temperature, basal (0001) <11–20> slip is easy to activate [12]. Non-basal slip requires higher critical resolved shear stresses (CRSS) [13], while prismatic {1–100} <11–20> slip is easier to activate than pyramidal {11–22} <11–23> slip [14]. The non-basal slip initiation affects the basal texture, which changes during deformation. However, most of the specimens molded in rare earth–magnesium alloys used for the study were deformed. Microstructure evolution before and after deformation, changes in long-period stacking ordered (LPSO) phases, and microstructure–property relationships are commonly explored. Breakthroughs have also been made for rare earth element-induced texture changes and even strong anisotropy due to strong texture. However, for rare earth–magnesium alloys, the study of the deformation mechanism in the deformation process is not yet very complete. As a result, the EBSD technique is used in this paper to analyze the deformation behavior during forging and extrusion deformation. This analysis primarily focuses on the DRX mechanism, twinning and slip behavior, texture evolution, and factors affecting texture weakening. Furthermore, the property-strengthening mechanisms are analyzed quantitatively.

2. Materials and Methods

The Mg-7Y-5Zn-0.1V (mass fraction) alloy was prepared using the ordinary casting method. The raw materials were high-purity magnesium (mass fraction: 99.99%), Zn (mass fraction: 99.99%), V (mass fraction: 99.99%), and Mg-30Y (mass fraction: 99.99%) master alloys. The melting process was guaranteed to be carried out with argon (Ar_2) gas. Then, the melt was achieved in a copper mold. After homogenization at 500 °C for 24 h, the alloy was obtained via cooling with water. Then, the specimen was cut to a diameter of 60 mm and a height of 120 mm, and it was preheated at 450 °C for 1 h before forging in YD1532 32S-400. The strain rate was 0.1 s^{-1}, and the final strain was 0.69. Finally, the extruded alloy was obtained by extruding the forged sample. The extruding ratio was 16, the extruding temperature was 350 °C, and the ram speed was 1 mm/s.

The microstructure was characterized using an optical microscope (OM, LeicaDM2700 M, Leica, Wetzlar and Mannheim, Germany) and a scanning electron microscope (SEM, Schaefer SEE Srl, Rovigo, Italy, TESCAN-MIRA3, PVD Laboratory, Tescan, Czech Republic). The microstructure conditions, such as texture, were analyzed using a TescanMira3 EBSD (TESCAN, Warrendale, PA, USA), and the elemental composition of specific areas was analyzed via SEM with energy dispersive spectroscopy (EDS) (Thermo Fisher Scientific, Waltham, MA, USA). The phase composition was measured with an X-ray diffractometer (XRD, Y-2000 type, Alvord Systems Inc., Clairton, PA, USA). According to the GB/T 228.1-2010 standard [15], the specimens were cut. Tensile tests were carried out using an electronic universal material test machine (INSTRON5969, Instron corporation, Norwood, MA, USA) at room temperature. The tensile rate was 0.2 mm/min. The tensile specimen direction was parallel to the forging and extrusion directions, respectively. In order to ensure the accuracy and reliability of the experimental data, tensile tests were conducted 3 times to take the average value.

3. Results

3.1. Microstructure Prior to Forging

Figure 1a,b show the SEM images of the forged alloy in the preheated state before forging, and Figure 1c shows the XRD of the alloy. In the Mg-Y-Zn-V alloy, the microstructure is composed of an a-Mg matrix, $Mg_{12}YZn$ (LPSO phase), and $Mg_3Zn_3Y_2$ (W phase). The compositions of points A, B, and C in Figure 1b are shown in Figure 1d, respectively. Combined with XRD and composition, both the A and C phases are $Mg_3Zn_3Y_2$. The gray contrast phase (marked as "B") is mainly composed of Mg, Y, and Zn elements, and the atomic ratios of Y to Zn are close to 1:1; this phase is indicated to be the LPSO phase [16]. In addition, lamellar phases can be seen within the crystal; they are lamellar LPSO phases (14H-LPSO) formed via the heat treatment process [17]. The alignment of these second-phase particles is not perfectly straight. It is curved and jagged in some regions, a phenomenon that has been confirmed by Mohammad Saadati [18], and the precipitates are strain-induced precipitates. The formation of parallel-aligned precipitation particles inside the grains has been reported. The precipitation particle precipitation strengthening mechanism can now be explained with three points [18]: (1) precipitation at certain specific planes, (2) precipitation at the slip bands, and (3) precipitation at the structural-layer misalignment of LPSO.
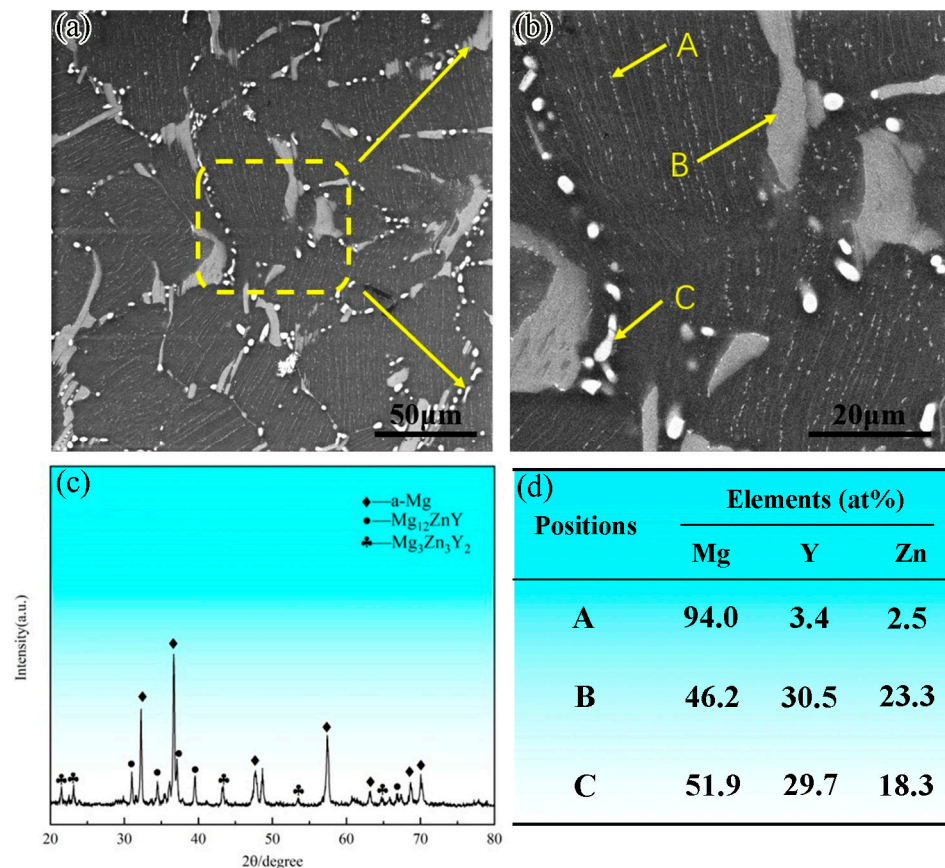

Figure 1. The forged Mg-Y-Zn-V alloy was preheated at 450 °C for 1 h: (**a**,**b**) SEM map, (**c**) XRD pattern, and (**d**) EDS.

In Mg-Y-Zn-V alloys, static or dynamic precipitation leads to the formation of W-phase particles, respectively, and most of these particles are parallel. Documents about rare earth–magnesium alloys show that the specific crystal surface of the α-Mg matrix is precipitated and grows up. Although these precipitates are directed along a certain crystal orientation of the α-Mg matrix, their formal nucleus occurs in a random position, rather than in a continuous form. Therefore, specific planes are not the only reason to explain the formation of these second-phase particles.

The intracrystalline bending phenomenon is a behavior of the LPSO structure reported by Lu et al. [19] and Yamasaki et al. [20]. In this experiment, the 14H-LPSO structure precipitated within the crystal and the precipitated particles were probably nucleated at the 14H-LPSO stacking layer dislocations. In addition, samples that were not deformed via a preheating treatment before deformation, in which no slip bands were generated, also formed parallel-aligned precipitation particles.

Furthermore, according to Zheng [21] and Yamasaki [22], it was shown that solute elements tend to precipitate at the LPSO's SFs and lead to the LPSO growing in different directions. From a thermodynamic and kinetic perspective, the supersaturated solid solution alloy was kept at 450 °C for a holding preheat of 1 h. Such a holding time is sufficient to nucleate these precipitated phases, leading to the precipitation of the W phase. Therefore, it can be concluded that these precipitated particles formed on the LPSO structure.

3.2. Microstructure after Deforming

3.2.1. SEM Analysis of Deformed Alloys

Figure 2a,d show that in the forged alloy, microstructure, and 18R are elongated along the ED direction and that more nanoscale W-phase and lamellar 14H-LPSO-phase precipitate was present inside the a-Mg matrix compared with the preheated alloy. Figure 2b,e are SEM images of forged-extruded alloy along the ED direction. They show that, although some elongated LPSO phase still exists, fragmentation occurs on the whole, and the W phase is finer and more dispersed. Figure 2c,f are SEM images of the forged-extruded alloy perpendicular to the ED direction. They show that the 14H-LPSO phase inside the grain is coarser and exhibits strong anisotropy, and it even has different degrees of twist. The grain is more refined near the LPSO phase.
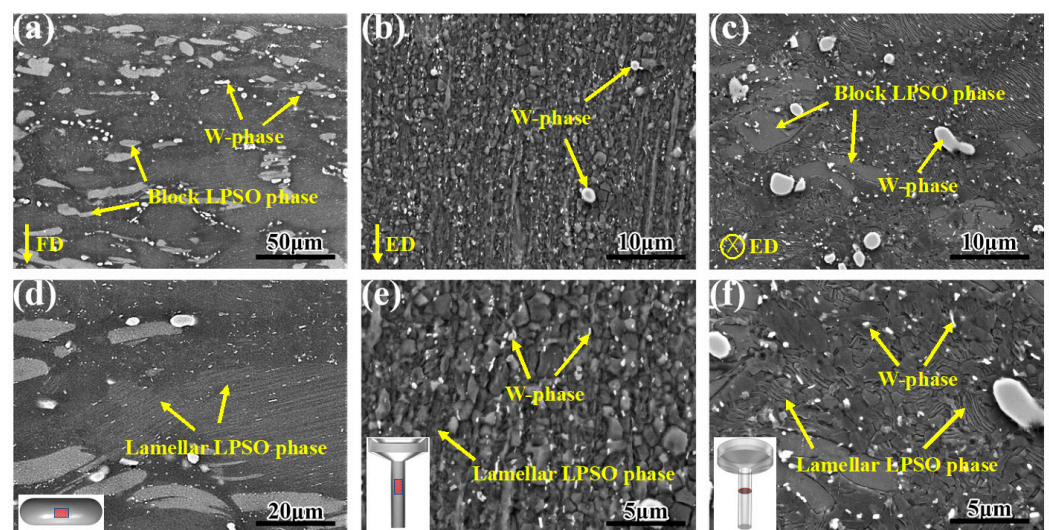

Figure 2. SEM images of Mg-Y-Zn-V alloy: (**a**,**d**) forged alloy, (**b**,**e**) extruding direction of the extruded alloy, and (**c**,**f**) vertical direction of the extruded alloy.

Relative to preheating during the state of precipitation static, the dynamic precipitation of the forging process for the second phase provides power, and combined with prior to the second-phase precipitation static, the Zn and Y elements had spread. As a result of the intracrystalline white particles, precipitate easily occurred in the LPSO structure place, and the forging process for the diffusion of solute atoms provided the power to further promote the proliferation of atomic migration. At the same time, part of the 14H-LPSO structure was bent and twisted in the forging process, and dislocation migration was hindered near the deformation of the LPSO phase, leading to cross-entanglement. Solute atoms were more likely to be enriched at the intersection of dislocation and SFs, so the interaction and

entanglement between dislocations promoted precipitation, nucleation, and growth in the forging process.

3.2.2. EBSD Analysis of Deformed Alloys

Figure 3 shows the inverse polar figure (IPF) map and grain orientation spread (GOS) maps of the deformed alloys. For a rare earth–magnesium alloy, the LPSO phase cannot be scanned using the instrument, so the unrecognized regions are considered to be LPSO phases. As the degree of deformation of the alloy increases, the grain becomes finer, as displayed in Figure 3a,c. After forging, DRX grains mainly occur in the large grains with jagged grain boundaries, belonging to the DDRX. DDRX can also be observed in Figure 3c, forming a partially bimodal microstructure, i.e., DRX grains surrounded deformed grains. To analyze the DRX behavior, DRX grains can be identified using GOS values (GOS < 1°) [23]. In Figure 3b,d, the area of the blue region increases significantly with an increasing degree of metamorphism, which explains the increase in the DRX score. The corresponding statistics for DRX scores were 7.5% and 45.3%. In addition, Figure 3b,d shows that deformed grains have different degrees of intragranular deformation, which also laterally suggests that perhaps substructures have appeared within the deformed grains.
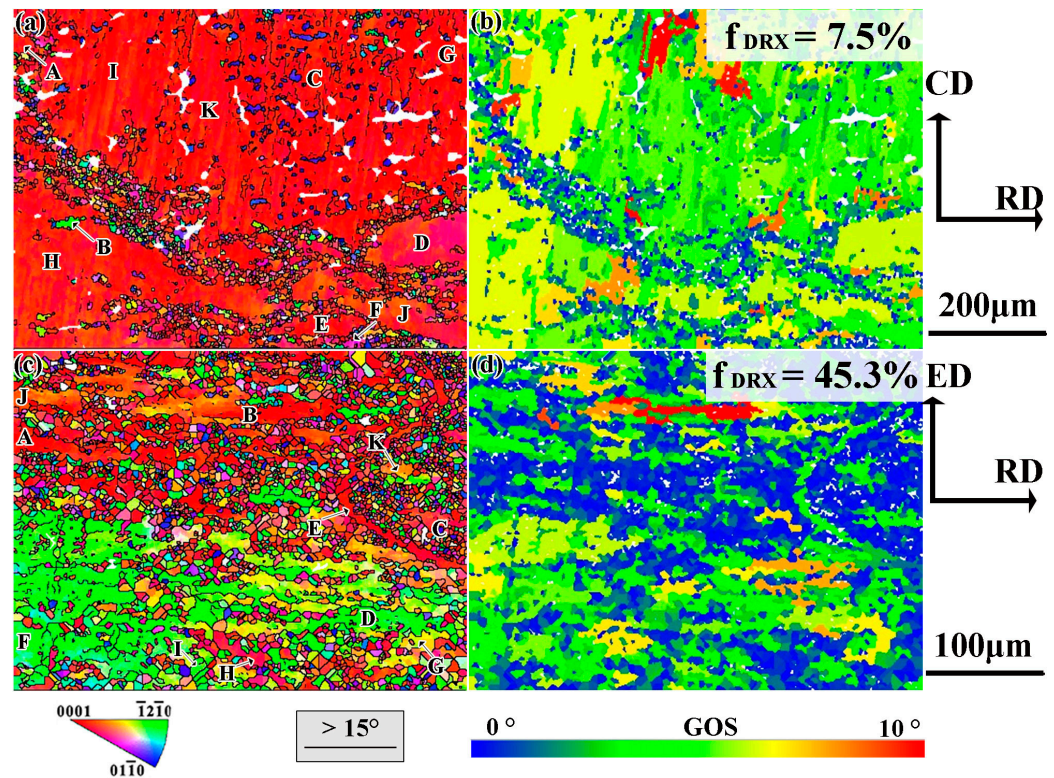

Figure 3. EBSD results of (**a**,**b**) forged and (**c**,**d**) extruded alloys: (**a**,**c**) IPF map and (**b**,**d**) GOS map.

The kernel average misorientation (KAM), the misorientation angle distribution, and the KAM value distribution map are displayed in Figure 4. The absence of protruding peaks without particularly pronounced angles in Figure 4a,b suggests that there are not many corresponding twins within the alloy. A decrease in low-angle grain boundaries (LAGB) is caused by DRX occurrences. Figure 4c,d are KAM plots showing the distribution of a large number of green areas, which are caused by lattice distortions and represent the increase in dislocations, revealing the occurrence of sufficient slip [24,25]. To further reveal the variation in dislocation density, the geometrically necessary dislocation (GND) can be quantitatively analyzed based on the following formula [26,27]:

$$\rho^{GND} = \frac{2KAM_{avg}}{\mu b},$$

(1)

where KAM_{avg} is the average KAM value; see other ref. [26]. The ρ^{GND} values are calculated to be 7.292×10^{15} m^{-2} and 5.833×10^{15} m^{-2}, corresponding to the alloys after forging and extrusion, respectively. As the degree of deformation of the alloy increases, the green area fraction decreases, and a corresponding decrease in dislocation density is observed. The reduction of the green area in Figure 4d indicates the release of stresses within the grain. Deformation energy is stored in the form of the accumulation of dislocations to provide energy for DRX nucleation [28]. When the ρ^{GND} reaches the threshold, the dislocations are depleted, leading to DRX formation and a decrease in ρ^{GND}. Meanwhile, LAGB take up dislocations to become high-angle grain boundaries (HAGB), leading to a decrease in LAGB [29].
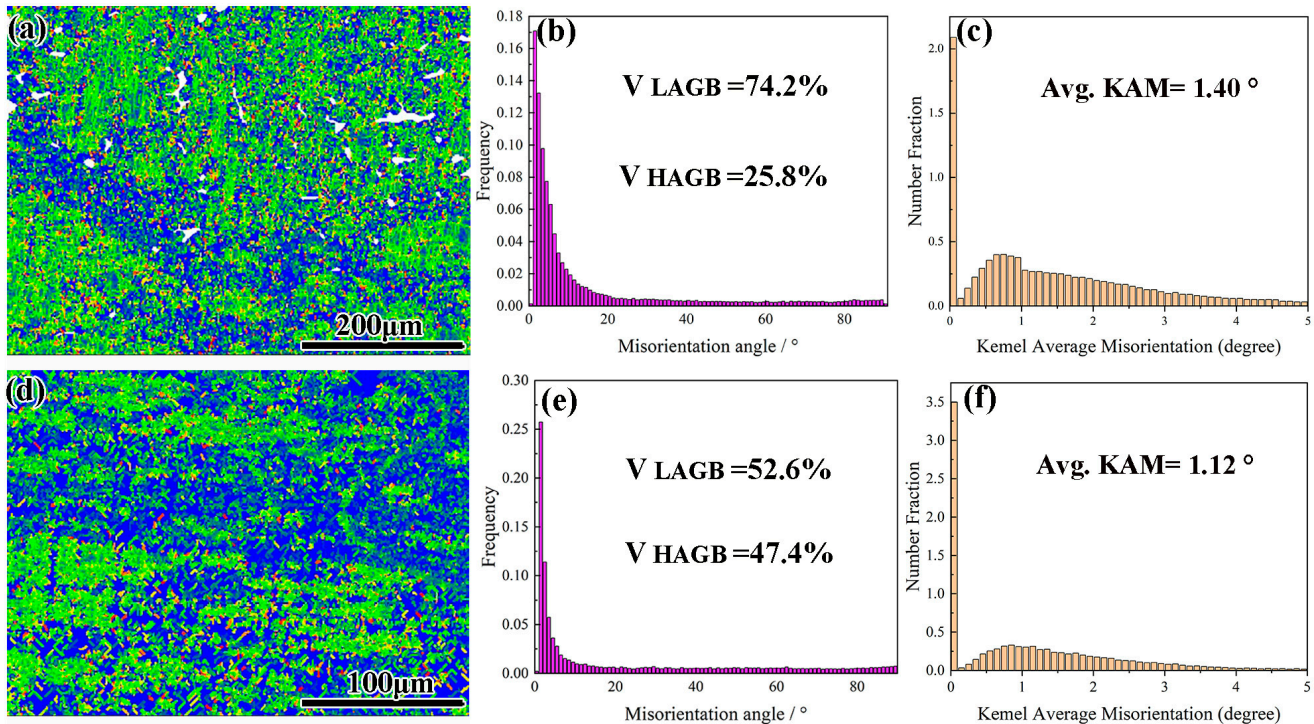

Figure 4. The KAM map, the misorientation angle distribution map, and the KAM value distribution map: (**a**–**c**) forged and (**d**–**f**) extruded alloys.

Figure 5 shows the pole figures (PFs) and the IPF map of the deformed alloy in different deformation states, which facilitates the exploration of the texture changes during deformation. Due to the lack of a uniform maximum value for the intensity of the texture, it is possible that the color and intensity do not match well (e.g., Figure 5d–f). Figure 5a–c are PF maps of the alloys after forging, and Figure 5d–f show PF after extruding. In Figure 5a,d, the typical strong basal texture disappears after extruding, the reorientation of the pole density point occurs, and the pole density points near TD, forming the (0001)//TD component texture. Changes in the basal texture can be attributed to DRX formation, the initiation of a non-basal plane slip, and twin activation. The effect of DRX formation on the strength of the basal texture, such as DDRX formation, cannot be ignored. This will be described in the discussion section. However, for Figure 5a–c, the basal texture of the un-DRX and all grains change little, and the strength increases slightly. In contrast, the extreme density points of DRX grains are dispersed, which explains the decrease in the basal texture strength of all grains compared to the non-DRX grains. After extruding, the texture exhibits the same trend, which is not elaborated upon here. Additionally, in Figure 5g, the emergent texture after forging is located between <−12−10> and <01−10>, while Figure 5h shows the typical texture after extruding, i.e., the <01−10>//ED texture component.
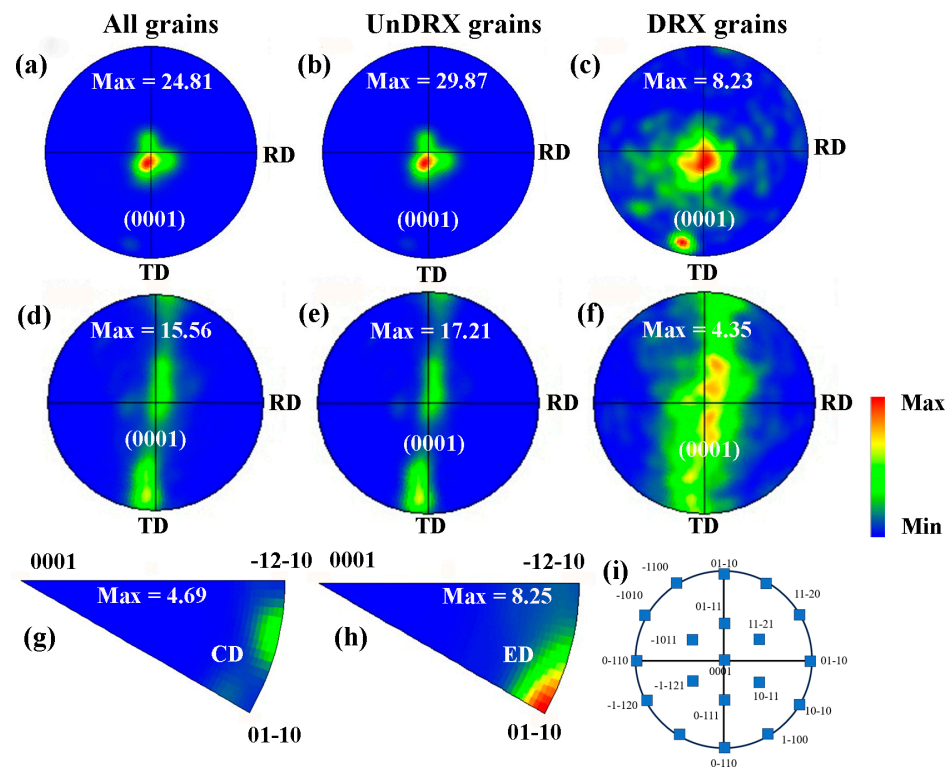
Figure 5. (**a**–**f**) PF map and (**g**,**h**) IPF map of forged and extruded alloys: (**a**–**c**,**g**) forged alloy and (**d**–**f**,**h**) extruded alloy. (**i**) {0001} ideal texture component of PF diagrams.

Since there are no special angular peaks in the misorientation angle distribution map, it is not possible to identify the presence of twins well, so we decided to explore the twins separately. The grain boundary (GB) diagram with twins is shown in Figure 6. The HAGB is represented with a black line, the {10–12} twin with a red line, the {10–11} twin with a blue line, and the {10–12}–{10–11} twin with a green line. The results show that the number of twins is not very high either after forging or after rolling. Only TTW exceeds 1% and is predominantly distributed within the deformed grains. Secondly, some of the twins are extended within the grain and show a tendency to split the parent grains. In order to confirm these twin types, the misorientation angles of each type of twin are shown in Figure 6a,b, respectively, and the results are displayed in Figure 6c,d.

Based on the above findings, {10–12} twins predominated in all alloys after forging and rolling. Consequently, we selected the typical regions in Figure 3a,c to specifically study {10–12} twinning behavior. It is important to note that the black line represents HAGB (>15°), the red line represents TTW, and the white line represents the LAGB (2~15°). All TTW variants and interrelationships can be found in Ref. [30]. The illustration is in Figure 7k below. Figure 7a,b show the DBSD results with four twin variants and a large number of LAGBs. From Figure 7a, it can be noticed that the twins are dispersed and nucleated, and the twins marked T1–T4 show irregular shapes instead of the symbolic lenticular morphology. Some of the twins are separated by the LAGB, which is also a precursor to CDRX. The orientations of the twin variants are similar, and since the angle of deflection between the variants is small, we regard them as the activation of a twin variant. Meanwhile, the boundary of some of the twins was identified as HAGB, which may indicate dislocation–twin interaction [31]. From Figure 7c–e, we can learn the crystal orientation relationship of the twin variant. The position relationship for the twin and parent crystals is displayed in Figure 7f. We regard the activation of T1, T2, and T4 as a type of twin variant since the EBSD data in Figure 7b demonstrate that T1 and T2 have the same crystal orientations, while T4 is challenging to identify due to its similar orientation and tiny deflection angle. However, two twin variants were determined to be activated in

Figure 7b, which show a meta-position relationship (schematic shown in Figure 7j). The growth of different variants collides, and the boundaries of the twin variants at the collision site appear serrated, which may be the result of the interaction of different twin variants. It is noteworthy that the twinned variant marked T4 was found to be divided into different parts by sub-boundaries, which is suggestive of subgrain production and suggests that twins make an important contribution to the formation of new grains. The crystallographic orientations and relationships of the different twin variants are shown in Figure 7g–i.
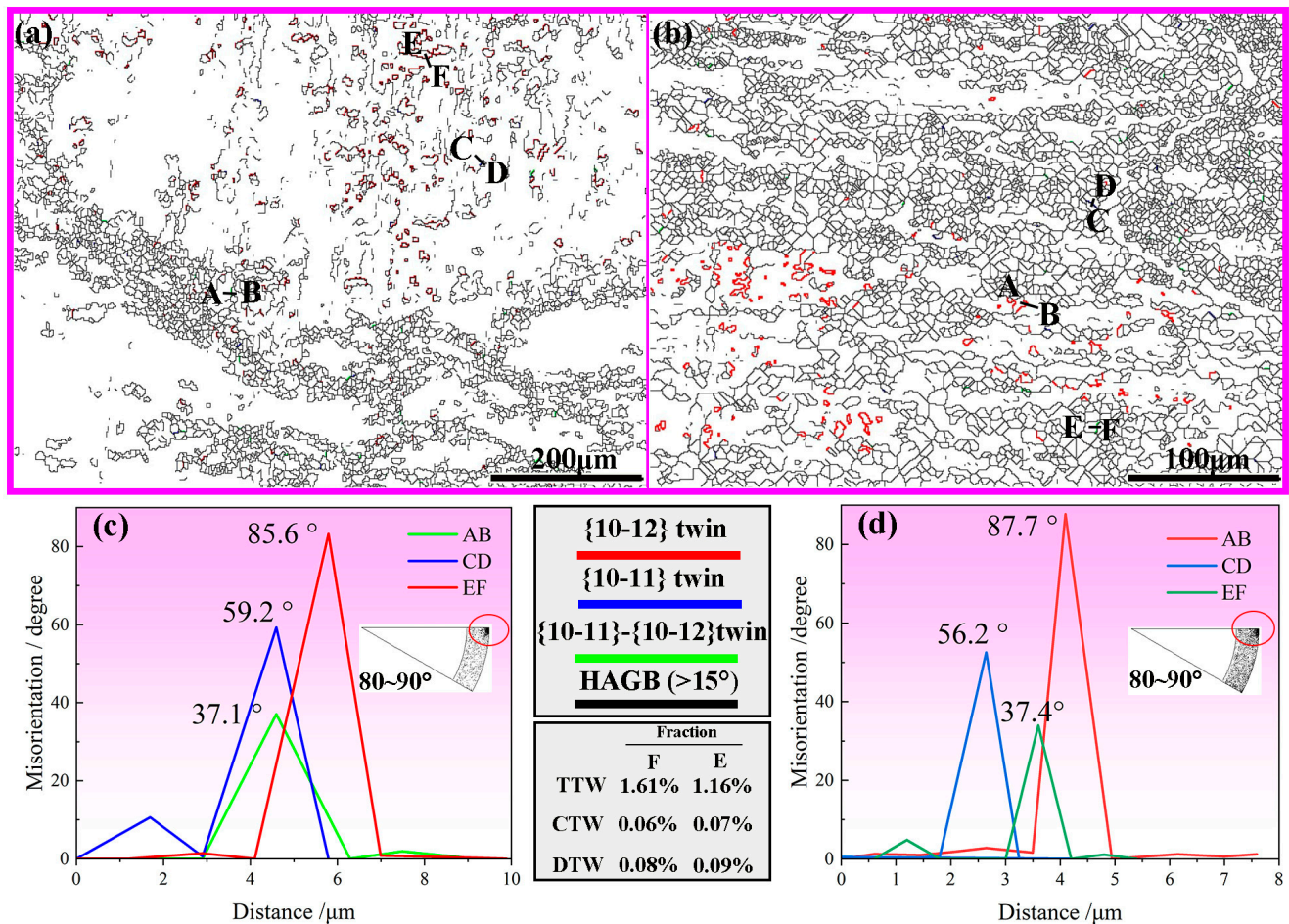

Figure 6. (**a**,**b**) GB map and (**c**,**d**) misorientation angle of forged and extruded alloys: (**a**,**c**) forged alloy and (**b**,**d**) extruded alloy.

It was mentioned that the changes in the texture may be affected by the slip system, so selecting some deformed grains in Figure 3a,b to study the slip behavior specifically. In order to accurately select deformed grains, deformed and DRX grains were recognized by their GOS values. And grains with a GOS > 1° were recognized as deformed grains. In order to further investigate the types of slip modes, the IGMA was used to identify the activation type. IGMA analyzes the slip by combining it with the Taylor axis, as detailed in Ref. [32]. The Taylor axis can be determined by the following geometric relationship [20,33]:

$$T = \gamma s \times n, \tag{2}$$

The results of the calculations are shown in Figure 8. Deformed grains with GOS > 1° were selected for this IGMA analysis, and the selected grains are marked accordingly in Figure 3a,b. The misorientation axes for object–point pairs with angles between 1° and 2° were chosen for this IGMA because angles above 2° have little influence on the qualitative difference characteristics of the IGMA. In order to analyze the activated slip

modes accurately, the magnitude of the Schmidt factor (SF) was analyzed for the different slip modes for all the grains selected, and all the SF values are displayed in Table 1.
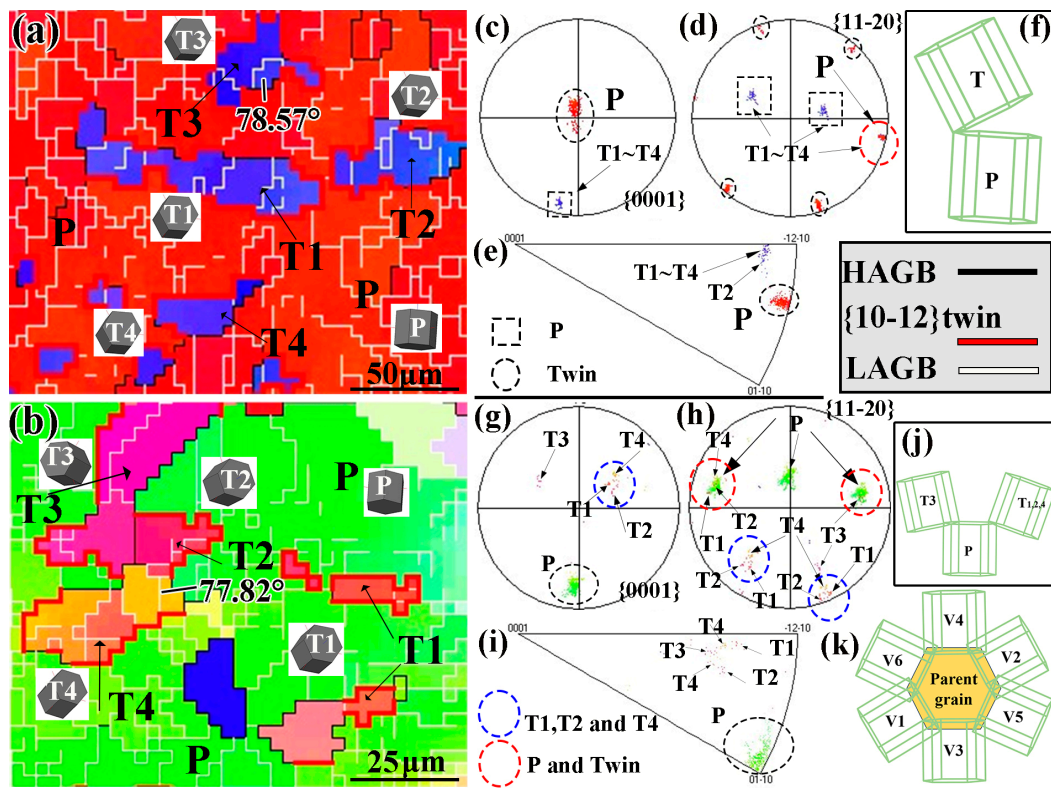

Figure 7. IPF map of (**a**) forged and (**b**) extruded alloys, (**c,d**) PF map and (**e**) IPF map of (**a**), (**g,h**) PF and (**i**) IPF map of (**b**), (**f,j,k**) schematic map of twin variant.

Table 1. Schmidt factor values for the three slip systems of corresponding grains.

Grains	<a> Basal		<a> Prismatic		<c+a> Pyramidal	
	Forged Alloy	Extruded Alloy	Forged Alloy	Extruded Alloy	Forged Alloy	Extruded Alloy
A	0.34	0.25	0.03	0.36	0.26	0.13
B	0.35	0.41	0.24	0.05	0.38	0.47
C	0.29	0.38	0.21	0.18	0.38	0.41
D	0.48	0.38	0.10	0.41	0.33	0.39
E	0.40	0.18	0.04	0.40	0.35	0.15
F	0.36	0.27	0.21	0.12	0.27	0.28
G	0.21	0.46	0.12	0.22	0.20	0.37
H	0.39	0.47	0.06	0.24	0.29	0.40
I	0.15	0.34	0.02	0.19	0.46	0.43
J	0.46	0.28	0.11	0.45	0.37	0.27
K	0.48	0.41	0.12	0.22	0.36	0.35

The IGMA is concentrated at the <0001> axis, which can be identified as the prismatic <a> slip initiation based on the results in Figure 8. The basal <a> and pyramidal <c+a> slip modes are activated when the IGMA is primarily focused on the <uvt0> axis [33]. IGAM distributions with intensity values exceed 2 mud are thought to have a preferred

IGMA distribution, otherwise having a uniform IGMA distribution [33]. Figure 9 shows the results of different grain IGMA distributions after forging. The results show that the IGMA distribution is mainly concentrated at the <vut0> axis and the intensity of the distribution is >2°, with preferential IGMA distribution at the <vut0> axis, which indicates the basal <a> and pyramidal <c+a> slip initiation. According to SF values (Table 1), the values for the basal <a> slip system are relatively higher, indicating that the dominant slip is basal slip. For individual grains (B, F, and G), the high-strength IGMA distribution is not concentrated in the <uvt0> axis. For example, for grains B and G, IGMA is concentrated in the <10–12> axis, suggesting pyramidal <a> slip initiation. Compared to IGMA distribution after forging, it changes considerably after extruding. Figure 10 shows the results of the IGMA distribution after extruding. The results show that some grains (e.g., E and J) are <0001> axis and have intensity values >2°, which suggests activation of prismatic <a> slip modes, according to the matched Taylor axis results in Figure 8. Some grains (e.g., B, D, F, and K) exhibit a uniform IGMA distribution, which may indicate the result of multiple slip modes dominating together. For grains with preferential IGMA distribution in the <uvt0> axis, activation of the pyramidal <c+a> slip mode is more likely by comparing the SF values across grains. Based on IGMA analysis, the basal <a> slip mode is predominant, followed by pyramidal <c+a> slip during forging. Besides prismatic <a>, pyramidal <c+a> and <a> slip are activated during extruding, which can be used to explain the changes in basal texture after extrusion.

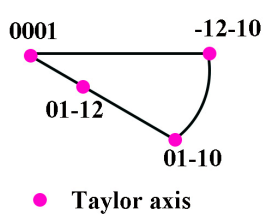| Slip mode	Slip type	Taylor axis	No. of variants of Taylor axis	
{0001}<11-20>	Basal <a>	<1-100>	3	
{10-10}<1-210>	Prismatic <a>	<0001>	1	
{10-11}<1-210>	Pyramidal <a>	<10-12>	6	
{11-22}<11-23>	Pyramidal <c+a>	<-1100>	3	

Figure 8. Slip systems in Mg alloys and their corresponding Taylor axes (Taylor axes of common slip systems are marked in red circles).
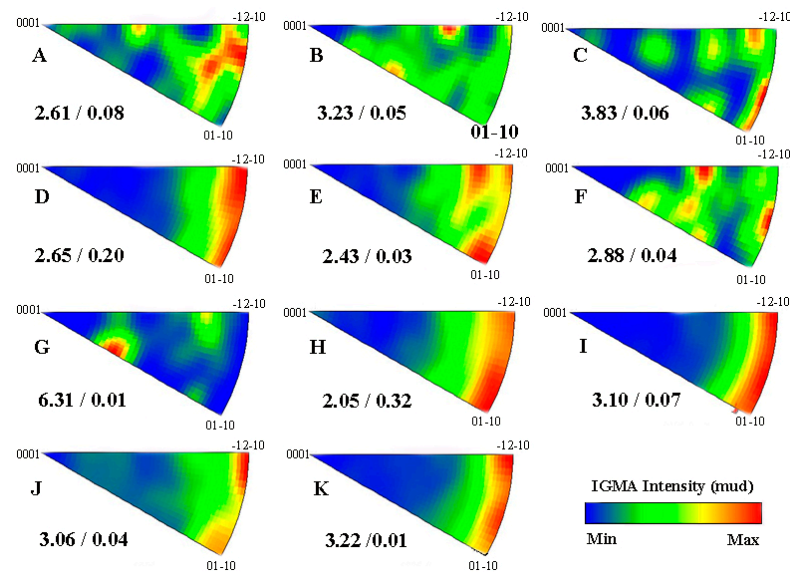

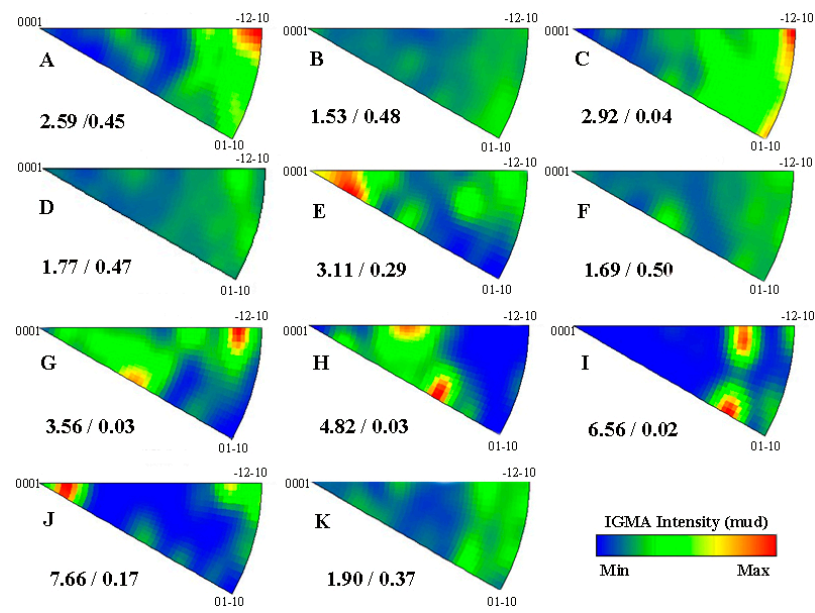**Figure 9.** The EBSD analysis of the IGMA results corresponding to Figure 3a ((**A–K**) are marked in Figure 3a).

Figure 10. The EBSD analysis of the IGMA results corresponding to Figure 3c ((**A–K**) are marked in Figure 3c).

3.3. Mechanical Properties of the Deformed Alloys

Figure 11 shows that the TS, UTS, and EL of the forged alloy are 200.5 MPa, 275.2 MPa, and 11.5%, respectively. The properties of the extruded alloy reached 340.1 MPa, 370.5 MPa, and 15.6%, respectively. Based on the analysis of the above results, the increase in strength was the result of the synergistic effect of various factors. Reinforcement mechanisms will be analyzed next.
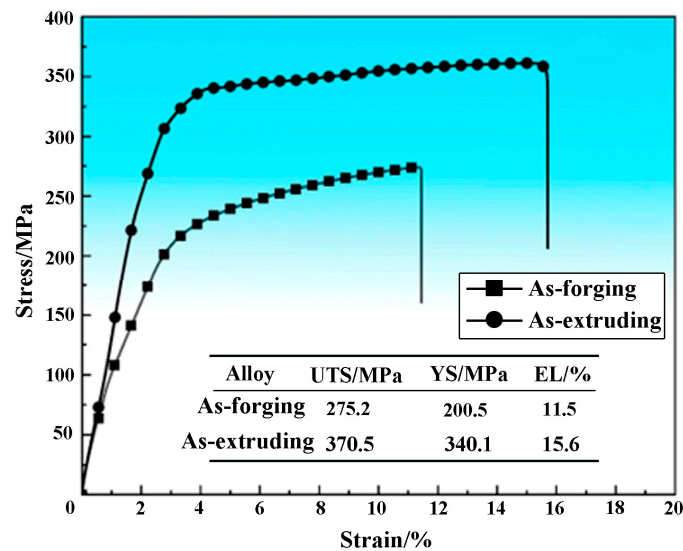

Alloy	UTS/MPa	YS/MPa	EL/%
As-forging	275.2	200.5	11.5
As-extruding	370.5	340.1	15.6

Figure 11. Tensile properties of the Mg-Y-Zn-V alloy at room temperature.

4. Discussion

4.1. Analysis of the DRX Mechanism

DRX mechanisms include DDRX, CDRX, and twin-induced DRX. The twins are mainly TTWs in this paper, and TDRX behavior was not observed. Du et al. claimed that DRX is more likely to nucleate near CTW and secondary CTW GBs while not near TTW and TB [34]. Since CTWs and secondary CTWs are less than 0.1%, this may affect the occurrence of TDRX. The observation of the presence of substructures within the twin grains in Figure 7b

does not account for the TDRX behavior and acts similarly to the twin grains splitting the parent grains, acting as a grain refinement.

Figure 12 shows the EBSD result of selected areas from Figure 3a. In Figure 12a, the bulging and necklace-like GBs can be observed. The bulging GBs are caused by the difference in dislocation density near the primal HAGB, as can be seen in Figure 12b (KAM map). During deformation, the initial LAGBs' bulging position will be used as the DRX nucleation position [35], which transforms into HAGBs in the high-strain and dislocation density region. This typical microstructural feature of bulging GBs suggests that the DRX mechanism of the alloy contains DDRX [36]. Figure 12c (GOS plot) ensures that our selected region contains DRX grains. In addition, serious lattice distortion was found in the P2 deformed grains in Figure 12a, and the presence of the CDRX phenomenon within the deformed grains was analyzed using the misorientation angle between AB and CD. The misorientation angle fluctuation of the P2 grains is depicted in Figure 12d. The findings indicate that the maximum accumulation of the misorientation angle is less than 15°, which may imply the tendency of the LAGBs to absorb dislocations' shift to the HAGBs. However, no HAGBs or new DRX grains formed, which is not characteristic of CDRX.
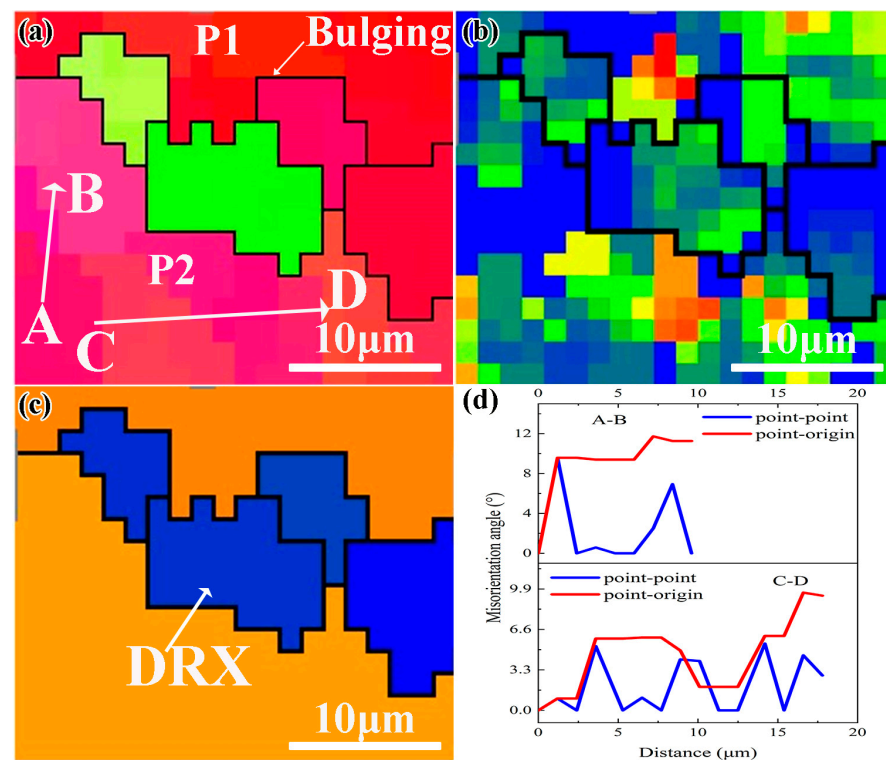

Figure 12. (**a**) IPF map, (**b**) KAM map, (**c**) GOS map, and (**d**) misorientation angle of AB and CD.

Figure 13 shows IPF, KMA, and GOS maps for regions selected from Figure 3c. The GOS map ensures that the region contains both DRX and non-DRX grains, which facilitates the study of the DRX mechanism during deformation. Prior to the formation of LAGBs, there is usually a recovery process associated with the generalized annihilation and rearrangement of dislocations [7]. CDRX is a continuous process during which LAGB continuously absorbs dislocations to transform into HAGB and new grains. Figure 13a shows that the P grain undergoes an orientation change and is divided into substructures through a sub-boundary. As shown in Figure 13a,d, crystallographic orientation rotation along AB was observed, and the cumulative orientation difference angle from A to B exceeds 15°. The increase in the misorientation angle occurs mainly at LAGB. This feature reflects the evolution from LAGB to HAGB. In Figure 13b, AB is in a highly strained and dense dislocation zone, which provides the necessary factors for CDRX. When the sub-boundaries in Figure 13a are combined with their position in Figure 13b, it becomes evident that the

two sides of the boundaries are situated in distinct strain zones, and the gradient difference encourages the subgrain to rotate and form new DRX grains. This microstructural feature belongs to the DRX mechanism of CDRX [36]. Bulging GBs are found in Figure 13c, which is a microstructural feature that suggests the occurrence of a DDRX mechanism.
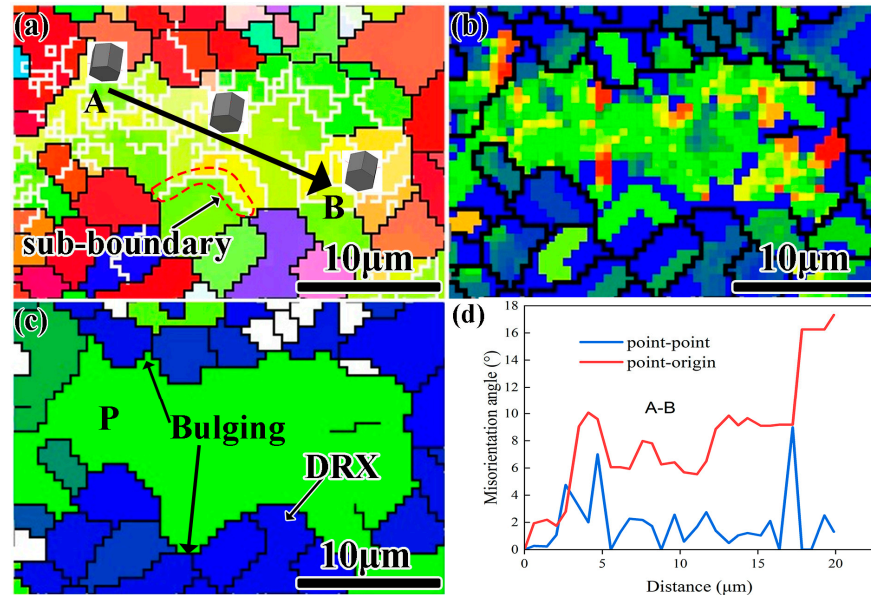

Figure 13. (**a**) IPF map, (**b**) KAM map, (**c**) GOS map, and (**d**) misorientation angle of AB.

The LPSO phase, as an important reinforcing phase in rare earth–magnesium alloys on DRX, cannot be neglected. Figure 14a,b shows the IPF and strain contouring maps for the selected region in Figure 3b. The strain contouring maps are used for stress analysis. Since LPSOs are not recognized during EBSD scanning, here, we consider the blanks (unresolved points) as LPSO phases. It was observed from Figure 14a,b that DRX is more adequate in regions of high stress. In the high-stress region, DRX grains appear next to the LPSO phase, which may indicate the occurrence of PSN-DRX [35]. Figure 14e,f illustrate a schematic representation of the PSN–DXR mechanism.
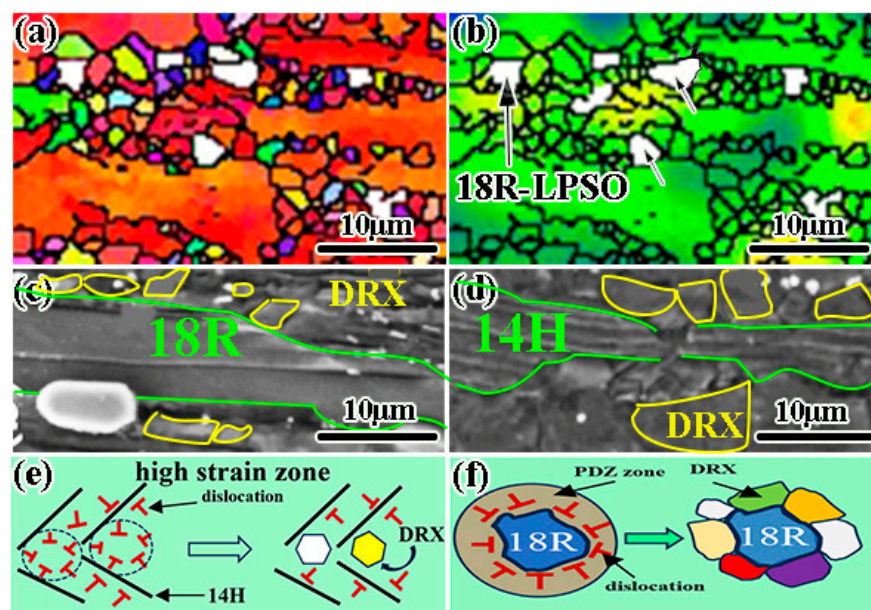

Figure 14. (**a**) IPF map, (**b**) strain contouring map, (**c**,**d**) SEM map, and (**e**,**f**) corresponding schematic.

4.2. Analysis of Twinning, Slip Behavior, and Texture Evolution

The main deformation mechanisms of Mg alloys are slip and twinning. According to the Von Mises rule, polycrystalline deformation requires five separate slip systems [37,38]. At low temperature, $CRSS_{basal} < CRSS_{twinning} < CRSS_{prismatic} < CRSS_{pyramidal}$ [39]. At the beginning of the deformation, the alloy exhibits a strong basal texture, as well as a basal slip-dominated deformed mode (from Figures 5 and 9), suggesting that basal slip dominates deformation during this period, with twinning and non-basal slip being of secondary importance. In Figure 11, the curves were found to be flat, which implies that twins are not the dominant plastic deformation mechanism but are involved in coordinated deformation. With increasing strain, grain refinement was observed, and the number of twins within the alloy was found to decrease. This phenomenon suggests that twins can more easily occur in coarse grains than in fine grains [35]. Fine grains can more easily coordinate deformation than coarse grains, and twins require higher activation stress than dislocation slip. Stresses concentrated at GBs are released, hindering the nucleation and growth of a twin [40]. By analyzing the IGMA, it was found that greater activation of non-basal slip modes occurred after extruding, which may affect the number of twins. In addition, more slip systems were activated, which is a factor that cannot be ignored for plasticity enhancement. In summary, basal slip dominates the deformation during forging, and prismatic and pyramidal slip are dominant deformation modes during extruding. A twin mainly coordinates the deformation during deformation.

Twins and DRX grains rotate the orientation of the crystals during deformation, which can have an effect on texture. The non-basal slip initiation also affects the basal texture. From Figure 5, it can be learnt that the basal texture is mainly determined by non-DRX, and the distribution of the extreme density points of DRX grains is a bit more dispersed, which suggests that the new DRX grains will probably reorientate. Due to the reorientation of DRX grains, the overall texture strength decreases compared to the non-DRX grain texture strength. In addition, Figure 5 shows that the basal texture changes after extruding compared to forging. This phenomenon is associated with a fuller DRX occurring after extrusion. In summary, DRX grains alter the components of texture and weaken the strength of texture. A twin also plays a role in the alteration of texture. It is known from Figure 7 that TTWs reorient from the parent grains and lead to an orientation difference with the parent grains. This phenomenon suggests that twinning changes the orientation of the parent grain during deformation, which affects the texture component. From the PF map in Figure 7, it can be learnt that the orientation pole density points of the twin deviate from the orientation pole density distribution of the parent crystal, which weakens the texture. In general, changes in the basal texture are more likely to be due to the prismatic <a> and pyramidal <c+a> slips' initiation [41–43]. From the IGMA analysis in Figure 10, the prismatic <a> and pyramidal <c+a> slip initiated during extruding can be used to explain the changes in the basal texture.

4.3. Analysis of the Strengthening Mechanism

(1)   Fine-grain strengthening

A finer grain indicates that more GBs will be formed. GBs enhance the properties of alloys by hindering dislocations. Fine-grain strengthening can be illustrated using the Hall–Petch refinement formula [44]:

$$\sigma_y = \sigma_0 + K_y d^{-1/2}, \tag{3}$$

d is the size of the grain, K_y is constant, σ_0 is friction stress, and σ_y is the yield strength. The d of the extruded and forged alloys is 1.7 μm and 11.8 μm, respectively. According to Equation (3), d is inversely proportional to YS. The contributed YS values of fine-grain strengthening in the forged and extruded alloys are 60.1 MPa and 175.2 MPa, respectively.

(2)   Load-transfer strengthening

The load transmission effect is a direct enhancement effect related to the enhanced phase (18R-LPSO). The loading stress in the α-Mg matrix can be transferred to the 18R-LPSO phase, thereby improving the strength. The load-transfer effect can be explained through the following formulas [45]:

$$\sigma_{Load} = \sigma_m \left[\frac{V_r(S+2)}{2} + V_m \right] \tag{4}$$

among them, S is the ratio of length and width, and V_m and V_r are the volume scores of the matrix and enhanced phase. Assuming 18R was broken under the action of cross-stress and the length and width ratio is 5. Under the load transmission effect of block 18R, the contributed YS values of the forged and extruded alloys are 26.5 MPa and 43.7 MPa, respectively.

(3)   Dislocation strengthening

During large plastic deformation, the incoherence deformation of the second-phase particles with the matrix results in an increase in dislocation density in the alloy, especially the forged alloy. Dislocation strengthening can be illustrated using the formula below [35]:

$$\sigma = \alpha G B \rho^{1/2} \tag{5}$$

where G is the shear modulus (1.66×10^4 MPa), the α value is 0.2, B is the Burgers vector (0.32 nm), and ρ is the dislocation density. Calculated using Equation (5), the contribution values of YS in the forged and extruded alloys are 51.5 MPa and 40.3 MPa, respectively.

(4)   Texture strengthening

Texture strengthening also affects the mechanical properties of the alloy. The formula below can explain texture strengthening [46]:

$$\sigma = m\tau_0 \tag{6}$$

where m is the Taylor factor related to the base texture, and τ_0 is the CRSS of the basal slip. For magnesium alloys with basal texture, the m value is 3.2 times the texture strength. The τ_0 value is 0.49MPa. The results (Figure 5) show that the texture strength is 24.80 and 15.56, respectively. According to Formula (6), the contribution values are 79.2 MPa and 50.3 MPa, respectively.

Based on all calculations, fine-grain strengthening and load-transfer strengthening have a positive effect on the YS increase after extruding. Compared to forging, both dislocation density and texture strength within the alloy are reduced after extruding, indicating that dislocation strengthening and texture strengthening do not contribute much to the increase in YS. However, the YS increase can be explained by the following formula (σ_A):

$$\sigma_A = \sigma_y + \sigma_{Load} \tag{7}$$

The theoretical values were found to be lower than the actual values using the formulas, which may be due to the fact that the selected characterization region does not give a good overview of the real situation inside the alloy. But the difference is not very great, and it is shown in Table 2.

Table 2. Contribution value of different strengthening mechanisms.

Alloy	σ_y (MPa)	σ_{Load} (MPa)	σ_A/Calculated (MPa)	σ_A/Actual (MPa)
As-extruding	115.1	17.2	132.3	139.6

5. Conclusions

(1)   As the degree of strain increased, the DRX region expanded, and the DRX mechanism transformed from DDRX into DDRX and CDRX.

(2)   During deformation, {10–12} tensile twins participated in plastic deformation as the main twins. As the degree of strain increased, a variety of {10–12} twin variants appeared and exhibited a meta-position relationship.

(3)   At the beginning of deformation, basal <a> slip dominated the slip mode and exhibited a strong basal texture. With increasing strain, prismatic <a> and pyramidal <c+a> slip initiated, and the basal texture transformed into the (0001)//TD component. Formed DRX grains and twins reorientated during deformation and weakened the texture.

(4)   Through deformation, the UTS and YS of the Mg-Y-Zn-V alloy were enhanced to 370.5 MP and 340.1 MPa, respectively. The enhancement of the strength was the result of the synergistic effect of multiple strengthening mechanisms.

Author Contributions: Conceptualization, C.Z., P.C. and W.L.; methodology, C.Z., P.C. and F.H.; validation, C.Z., F.H. and Q.S.; formal analysis, C.Z. and W.L.; writing—original draft preparation, W.L.; writing—review and editing, C.Z. and P.C.; data curation, Q.S.; funding acquisition, C.Z. All authors have read and agreed to the published version of the manuscript.

Data Availability Statement: The raw data supporting the conclusions of this article will be made available by the authors on request.

Conflicts of Interest: The authors declare that they have no known conflicting financial interests or personal relationships that could have appeared to influence the work reported in this paper.

References

1.   Yang, Y.; Xiong, X.; Chen, J.; Peng, X.; Chen, D.; Pan, F. Research advances in magnesium and magnesium alloys worldwide in 2020. *J. Magnes. Alloys* **2021**, *9*, 705–747. [CrossRef]

2.   Zhang, J.; Liu, S.; Wu, R.; Hou, L.; Zhang, M. Recent developments in high-strength Mg-RE-based alloys: Focusing on Mg-Gd and Mg-Y systems. *J. Magnes. Alloys* **2018**, *6*, 277–291. [CrossRef]

3.   Song, J.; She, J.; Chen, D.; Pan, F. Latest research advances on magnesium and magnesium alloys worldwide. *J. Magnes. Alloys* **2020**, *8*, 1–41. [CrossRef]

4.   Barnett, M.R. Twinning and the ductility of magnesium alloys. *Mater. Sci. Eng. A* **2007**, *464*, 1–7. [CrossRef]

5.   Christian, J.W.; Mahajan, S. Deformation twinning. *Prog. Mater. Sci.* **1995**, *39*, 1–157. [CrossRef]

6.   Li, H.; Mason, D.; Bieler, T.; Boehlert, C.; Crimp, M. Methodology for estimating the critical resolved shear stress ratios of α-phase Ti using EBSD-based trace analysis. *Acta Mater.* **2013**, *61*, 7555–7567. [CrossRef]

7.   Lu, S.H.; Wu, D.; Chen, R.S.; Han, E.H. The effect of twinning on dynamic recrystallization behavior of Mg-Gd-Y alloy during hot compression. *J. Alloys Compd.* **2019**, *803*, 277–290. [CrossRef]

8.   Prakash, P.; Toscano, D.; Shaha, S.K.; Wells, M.A.; Jahed, H.; Williams, B.W. Effect of temperature on the hot deformation behavior of AZ80 magnesium alloy. *Mater. Sci. Eng. A* **2020**, *794*, 139923. [CrossRef]

9.   Hong, S.G.; Park, H.; Lee, C.S. Role of {10–12} twinning characteristics in the deformation behavior of a polycrystalline magnesium alloy. *Acta Mater.* **2010**, *58*, 5873–5885. [CrossRef]

10.   Wang, X.; Jiang, L.; Cooper, C.; Yu, K.; Zhang, D.; Rupert, T.J.; Mahajan, S.; Beyerlein, I.J.; Lavernia, E.J.; Schoenung, J.M. Toughening magnesium with gradient twin meshes. *Acta Mater.* **2020**, *195*, 468–481. [CrossRef]

11.   Gui, Y.W.; Cui, Y.J.; Bian, H.K.; Li, Q.A.; Ouyang, L.X.; Chiba, A. Role of slip and {10–12} twin on the crystal plasticity in Mg-RE alloy during deformation process at room temperature. *J. Mater. Sci. Technol.* **2021**, *80*, 279–296. [CrossRef]

12.   Wang, Y.N.; Huang, J.C. The role of twinning and untwinning in yielding behavior in hot-extruded Mg-Al-Zn alloy. *Acta Mater.* **2007**, *55*, 897–905. [CrossRef]

13.   Agnew, S.R.; Duygulu, O. Plastic anisotropy and the role of non-basal slip in magnesium alloy AZ31B. *Int. J. Plast.* **2005**, *21*, 1161–1193. [CrossRef]

14.   Clausen, B.; Tome, C.N.; Brown, D.W.; Agnew, S.R. Reorientation and stress relaxation due to twinning: Modeling and experimental characterization for Mg. *Acta Mater.* **2008**, *56*, 2456–2468. [CrossRef]

15.   *GB/T 228.1-2010*; Metallic Materials—Tensile Testing—Part 1: Method of Test at Room Temperature. China Quality Press: Shanghai, China, 2016.

16.   Li, M.; Zhang, K.; Li, X.G.; Yuan, J.W.; Li, Y.J.; Ma, M.L.; Shi, G.L.; Li, T.; Liu, J.B. Effect of Zn on the microstructure and mechanical properties of as-cast Mg–7Gd–3Y–1Nd–0.5Zr alloy. *Mater. Sci. Eng. A* **2015**, *638*, 46–53. [CrossRef]

17.   Hao, J.Q.; Zhang, J.S.; Li, B.Q.; Xie, R.Z. Effects of 14H LPSO phase on the dynamic recrystallization and work-hardening behaviors of an extruded Mg–Zn–Y–Mn alloy. *Mater. Sci. Eng. A* **2021**, *804*, 140727. [CrossRef]

18. Saadati, M.; Khosroshahi, R.A.; Ebrahimi, G.; Jahazi, M. Formation of precipitates in parallel arrays on LPSO structures during hot deformation of GZ41K magnesium alloy. *Mater. Charact.* **2017**, *131*, 234–243. [CrossRef]

19. Lu, F.; Ma, A.; Jiang, J.; Yang, D.; Yuan, Y.; Zhang, L. Formation of profuse long period stacking ordered microcells in Mg-Gd-Zn-Zr alloy during multipass ECAP process. *J. Alloys Compd.* **2014**, *601*, 140–145. [CrossRef]

20. Yamasaki, M.; Hagihara, K.; Inoue, S.L.; Hadorn, J.P.; Kawamura, Y. Crystallographic classification of kink bands in an extruded Mg-Zn-Y alloy using intragranular misorientation axis analysis. *Acta Mater.* **2013**, *61*, 2065–2076. [CrossRef]

21. Zheng, L.; Liu, C.; Wan, Y.; Yang, P.; Shu, X. Microstructures and mechanical properties of Mg-10Gd-6Y-2Zn-0.6Zr (wt.%) alloy. *J. Alloys Compd.* **2011**, *509*, 8832–8839. [CrossRef]

22. Yamasaki, M.; Sasaki, M.; Nishijima, M.; Hiraga, K.; Kawamura, Y. Formation of 14H long period stacking ordered structure and profuse stacking faults in Mg-Zn-Gd alloys during isothermal aging at high temperature. *Acta Mater.* **2007**, *55*, 6798–6805. [CrossRef]

23. Dietrich, L.; Turski, K. A new method of thin sheets testing under compression. *Eng. Trans.* **1978**, *26*, 91.

24. Zhang, L.; Yuan, S.; Wang, J.; Chen, L.; Jin, P. Hot deformation behavior, processing map, microstructure evolution and dynamic recrystallization mechanism of Mg-5Al-0.6Sc alloy. *J. Alloy Compd.* **2022**, *922*, 166244. [CrossRef]

25. Victoria-Hernández, J.; Yi, S.; Letzig, D. Role of non-basal slip systems on the microstructure and texture development of ZXK-Mg alloy deformed in Plane Strain Compression at elevated temperature. *Scr. Mater.* **2022**, *208*, 114322. [CrossRef]

26. Ma, D.; Yuan, S.; Luan, S.; Jin, P.; Hu, H.; Wang, J.; Li, X. Hot deformation behavior, microstructure evolution and slip system of Mg-2Zn-0.5Mn-0.2Ca alloy. *J. Mater. Res. Technol.* **2022**, *21*, 164354. [CrossRef]

27. Cai, W.; Wang, C.; Sun, C.; Qian, L.; Fu, M.W. Microstructure evolution and fracture behaviour of TWIP steel under dynamic loading. *Mater. Sci. Eng. A* **2022**, *851*, 143657. [CrossRef]

28. Zhang, Q.; Li, Q.; Chen, X.; Bao, J.; Chen, Z. Effect of Sn addition on the deformation behavior and microstructural evolution of Mg-Gd-Y-Zr alloy during hot compression. *Mater. Sci. Eng. A* **2021**, *826*, 142026. [CrossRef]

29. Zhang, M.Y.; Zhang, Y.Q.; Yu, H.; Wang, H.X.; Niu, X.F.; Wang, L.F.; Li, H.; Cheng, W.-L. Revealing the deformation behavior and resultant texture evolution in extruded dilute Mg-Bi-Sn-Ca alloy during hot compression. *Mater. Sci. Eng. A* **2022**, *853*, 143788. [CrossRef]

30. Shi, Z.Z.; Xu, J.Y.; Yu, J.; Liu, X.F. Intragranular cross-level twin pairs in AZ31 Mg alloy after sequential biaxial compressions. *J. Alloys Compd.* **2018**, *749*, 52–59. [CrossRef]

31. Su, H.; Zhou, X.; Zheng, S.; Ye, H.; Yang, Z. Atomic-resolution studies on reactions between basal dislocations and {10–12} coherent twin boundaries in a Mg alloy. *J. Mater. Sci. Technol.* **2021**, *66*, 28–35. [CrossRef]

32. Chun, Y.B.; Battaini, M.; Davies, C.H.J.; Hwang, S.K. Distribution characteristics of in-grain misorientation axes in cold-rolled commercially pure titanium and their correlation with active slip modes. *Metall. Mater. Trans. A* **2010**, *41*, 3473–3487. [CrossRef]

33. Matsumoto, T.; Yamasaki, M.; Hagihara, K.; Kawamura, Y. Configuration of dislocations in low-angle kink boundaries formed in a single crystalline long-period stacking ordered Mg-Zn-Y alloy. *Acta Mater.* **2018**, *151*, 112–124. [CrossRef]

34. Du, P.; Furusawa, S.; Furushima, T. Continuous observation of twinning and dynamic recrystallization in ZM21 magnesium alloy tubes during locally heated dieless drawing. *J. Magnes. Alloys* **2022**, *10*, 730–742. [CrossRef]

35. Feng, Y.H.; Qian, L.Y.; Sun, C.Y.; Xu, S.N.; Zhu, N.; Wang, C.; Liu, Y. Twinning, dynamic recrystallization, and texture evolution in as-solution AZ80 Mg alloy during hot compression. *J. Mater. Res. Technol.* **2023**, *25*, 5159–5173. [CrossRef]

36. Jiang, M.G.; Xu, C.; Yan, H.; Fan, G.H.; Nakata, T.; Lao, C.S.; Chen, R.; Kamado, S.; Han, E.; Lu, B. Unveiling the formation of basal texture variations based on twinning and dynamic recrystallization in AZ31 magnesium alloy during extrusion. *Acta Mater.* **2018**, *157*, 53–71. [CrossRef]

37. Hao, M.; Cheng, W.; Wang, L.; Mostaed, E.; Bian, L.; Wang, H.; Niu, X. Texture evolution induced by twinning and dynamic recrystallization in dilute Mg-1Sn-1Zn-1Al alloy during hot compression. *J. Magnes. Alloys* **2020**, *8*, 899–909. [CrossRef]

38. Cheng, X.Y.; Yuan, Y.; Chen, T.; Zheng, Z.B.; Ma, L.F.; Jiang, B.; Tang, A.; Pan, F. The effects of second-alloying-element on the formability of Mg-Sn alloys in respect of the stacking fault energies of slip systems. *Mater. Today Commun.* **2021**, *29*, 102829. [CrossRef]

39. Chapuis, A.; Driver, J.H. Temperature dependency of slip and twinning in plane strain compressed magnesium single crystals. *Acta Mater.* **2011**, *59*, 1986–1994. [CrossRef]

40. Zhang, Q.; Pang, H.; Li, Q.; Gui, Y.; Chen, X.; Li, X.; Chen, P.; Tan, J. {10–12} twinning relationship in Mg-Gd-Y(-Sn)-Zr alloys under uniaxial compression at room temperature. *Mater. Sci. Eng. A* **2022**, *835*, 142679. [CrossRef]

41. Srinivasarao, B.; Dudamell, N.V.; Pérez-Prado, M.T. Texture analysis of the effect of non-basal slip systems on the dynamic recrystallization of the Mg alloy AZ31. *Mater. Charact.* **2013**, *75*, 101–107. [CrossRef]

42. Boehlert, C.J.; Chen, Z.; Gutiérrez-Urrutia, I.; Llorca, J.; Pérez-Prado, M.T. In situ analysis of the tensile and tensile-creep deformation mechanisms in rolled AZ31. *Acta Mater.* **2012**, *60*, 1889–1904. [CrossRef]

43. Styczynski, A.; Hartig, C.H.; Bohlen, J.; Letzig, D. Cold rolling textures in AZ31 wrought magnesium alloy. *Scr. Mater.* **2004**, *50*, 943–947. [CrossRef]

44. Yu, H.H.; Xin, Y.C.; Wang, M.Y.; Liu, Q. Hall-Petch relationship in Mg alloys: A review. *J. Mater. Sci. Technol.* **2018**, *34*, 248–256. [CrossRef]

45. Mabuchi, M.; Higashi, K. Strengthening mechanisms of Mg-Si alloys. *Acta Mater.* **1996**, *44*, 4611–4618. [CrossRef]
46. Bi, G.L.; Wang, Y.S.; Jiang, J.; Gu, J.R.; Li, Y.D.; Chen, T.J.; Ma, Y. Microstructure and mechanical properties of extruded Mg-Y-Zn (Ni) alloys. *J. Alloys Compd.* **2021**, *881*, 160577. [CrossRef]